

Full paper

A Raman spectroscopic study of graphene cathodes in high-performance aluminum ion batteries



Anthony S. Childress, Prakash Parajuli, Jingyi Zhu, Ramakrishna Podila*, Apparao M. Rao*

Clemson Nanomaterials Institute, Dept. of Physics and Astronomy, 118 Kinar Laboratory, Clemson University, Clemson, SC 29634, USA

ARTICLE INFO

Keywords:

Aluminum ion battery
In situ Raman spectroscopy
Graphene
Graphite intercalation compound
Nitrogen doping

ABSTRACT

Few layer graphene is a promising cathode material for aluminum-ion batteries that use chloroaluminate (AlCl_4^-) ionic liquids as the electrolyte. A fundamental understanding of interactions between the few layer graphene cathode and the ionic liquid electrolyte is key for realizing the full potential of these systems. Through in situ Raman spectroscopy and density functional theory calculations, we show that the cathode is capable of achieving stage-one intercalation within the operating voltage window, leading to improved cell performance. We also show that the presence of structural defects in few layer graphene such as pores induced via plasma exposure or nitrogen dopants can deteriorate the cell performance by either decreasing the electrical connectivity or precluding stage-one intercalation respectively. The cathodes made with highly crystalline few layer graphene display high power and energy densities ($\sim 200 \text{ W h kg}^{-1}$ at 200 W kg^{-1} and $\sim 160 \text{ W h kg}^{-1}$ at 5000 W kg^{-1}), and are stable with no loss in performance up to 1000 cycles while fully charging to 2.4 V.

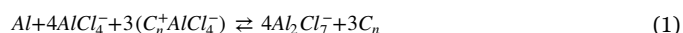
1. Introduction

Lithium ion batteries (LIBs) have become ubiquitous with regard to products such as mobile phones, laptop computers, and electric vehicles. They currently dominate the market for these applications and much research has been devoted in recent decades to improve LIB performance. However, for future battery applications that require high power as well as high energy densities, other architectures will be required. New alternatives (e.g., Li-S, Li-air) still rely on Li metal, which is potentially unsafe and whose reserves could be depleted in as little as fifty years if the demand for electric vehicles grows as expected [1]. Choosing newer materials beyond Li is imperative for replacing environmentally harmful and inherently volatile Li-chemistries. Aluminum, the most abundant metal in the Earth's crust ($\sim 8\%$ vs. 0.0065% for Li) [2], displays three-electron redox properties and a four-fold higher volumetric capacity than Li ($\sim 8040 \text{ mA h cm}^{-3}$ vs. $\sim 2000 \text{ mA h cm}^{-3}$). Thus, rechargeable Al-ion batteries (AIBs) are posited as safer and less expensive alternatives to existing Li-technologies if the present challenges such as graphite cathode disintegration, low cell discharge voltage, and insufficient cycle life with concomitant loss of capacity can be addressed [3–10].

Lin et al. recently addressed some of these issues by fabricating a stable AIB using 1-ethyl-3-methylimidazolium (EMI)- AlCl_4 ionic liquid

as the electrolyte and redox medium and replacing the standard graphite cathode with a three-dimensional few-layer graphene (FLG) foam [11]. Graphene and its derivatives have found abundant applications in energy storage research, and several recent review articles are available on the subject [12–15]. AIBs from Lin et al. demonstrated very fast charge rates ($\sim 4 \text{ A g}^{-1}$) and minimal capacity loss after 700 cycles. Notwithstanding this progress, the gravimetric energy density of these AIBs still remains far below that of LIBs. Unlike LIBs, little is known regarding the electrode redox reactions in AIBs, which is the main bottleneck in improving their performance to surpass LIBs. Specifically, the reaction and intercalation mechanisms between the EMI- AlCl_4 electrolyte and graphene layers still remain ambiguous, motivating our investigation through detailed spectroelectrochemistry.

The following reaction, which is consistent with past research into chloroaluminate ionic liquid chemistry [16–21], has been proposed in the literature to describe the redox and intercalation mechanisms in AIBs



where the discharge process is from left to right [3,11]. While charging, Al is plated onto the anode (Al metal) and AlCl_4^- ions intercalate into the cathode (FLG/graphite) lattice. During discharge, the AlCl_4^- ions leave the graphite host to react with the Al metal anode forming Al_2Cl_7^-

Abbreviations: AIB, aluminum ion battery; FLG, few layer graphene; GIC, graphite intercalation compound; EMICl, ethyl methylimidazolium chloride

* Corresponding authors.

E-mail addresses: childre@g.clemson.edu (A.S. Childress), pparaju@g.clemson.edu (P. Parajuli), jzhu2@g.clemson.edu (J. Zhu), rpodila@g.clemson.edu (R. Podila), arao@g.clemson.edu (A.M. Rao).

<http://dx.doi.org/10.1016/j.nanoen.2017.06.038>

Received 14 April 2017; Received in revised form 21 June 2017; Accepted 23 June 2017

Available online 24 June 2017

2211-2855/ © 2017 Elsevier Ltd. All rights reserved.

ions. These intercalation/de-intercalation processes in AIBs, which either limit the charge rates or expand the FLG/graphite cathode leading to disintegration, are poorly understood with contrasting theoretical explanations. For example, based on density functional theory (DFT) calculations, Jung et al. concluded that the pyramidal AlCl_4^- ions intercalate in FLG while retaining their geometry and also stack within the gallery space between the graphene sheets [22]. In contrast, DFT studies by Wu et al. suggested that AlCl_4^- ions may become planar when sandwiched between graphene layers, leading to an improved rate of ion diffusion through the cathode [23]. It has also been proposed that intercalation occurs via free Al^{3+} ions or Cl_2 molecules [5,6].

Here, we present a comprehensive spectroelectrochemical study, along with DFT calculations, to elucidate reactions at the cathode in AIBs with Al anode and FLG foam cathodes in EMI- AlCl_4 electrolyte.

The cyclic voltammograms (CVs) of our AIBs display three distinct redox processes that were concomitantly tracked using in situ Raman spectroscopy, providing insight into the intercalation/de-intercalation of the AlCl_4^- ions. DFT calculations are used to model the charge transfer between the graphene sheets and the AlCl_4^- ions, the results of which concur with our spectroscopic measurements. Based on these insights, we demonstrate graphene-based AIBs with the high energy and power densities ($\sim 200 \text{ W h kg}^{-1}$ at 200 W kg^{-1} and $\sim 160 \text{ W h kg}^{-1}$ at 5000 W kg^{-1}) that exhibit a slow decrease in energy at higher power densities.

In previous work, we showed that defects and dopants in FLG results in a shift of the Fermi energy as well as pores which allow better access to interior surface area leading to energy densities beyond the theoretical limit in graphene-based supercapacitors [24]. Motivated by this work, Yu et al. fabricated AIBs using FLG foam cathodes subjected to plasma processing [25], which exhibited low charge voltage (cutoff at 2.3 V), high capacity (123 mA h g^{-1} at current of 5000 mA g^{-1}), and excellent cycling ability due to defect and nanoribbon formation. Zhang et al. have reported that the diffusion of AlCl_4^- ions in FLG could be hindered due to carboxyl and hydroxyl functional groups at the edges of the basal planes through which the ions must pass [26]. Here we perform a systematic study to understand how plasma induced surface defects may influence the reactions at the cathode. We find that the energy and power densities of the FLG cathode, as well as the intercalation mechanism, are insensitive to in-plane surface defects as long as such defects do not significantly alter the electrical connectivity. Lastly, we investigate the effect of N-dopants on cell performance, partially motivated by the previous work on capacitors. Others have found that adding nitrogen to the graphene lattice is beneficial for cells relying on the intercalation of cations for the formation of donator-type graphite intercalation compounds (GICs) [27–29]. In contrast, we show that in our system that relies on anion intercalation the presence of N-dopants inhibits intercalation and leads to poor cell performance.

2. Materials and methods

Nickel foam (MTI Corp.) was used as the substrate for the synthesis of the FLG cathodes. Several pieces of Ni foam (dia. $\sim 16 \text{ mm}$, thickness $\sim 1 \text{ mm}$) were placed in a 1" diameter quartz tube furnace and first annealed at 900°C for one hour under flowing Ar (230 sccm) and H_2 (120 sccm). Next, the furnace temperature was reduced to 850°C , and methane (100 sccm) was introduced for one hour. The furnace was then cooled to 400°C under continued Ar flow, and allowed to dwell for two hours. The furnace was finally shut off and allowed to cool to room temperature in flowing Ar. For the N-doped FLG, acetonitrile vapors were introduced into the furnace for 20 min during the growth process by bubbling 50 sccm Ar through acetonitrile. The presence of N-dopants was confirmed using X-ray photoemission spectroscopy studies described elsewhere, which showed $\sim 2 \text{ at\% N}$ in FLG [24].

The mass of FLG was determined by weighing the Ni foam before and after the FLG growth using a Radwag micro balance. We found Ni foam (dia. $\sim 16 \text{ mm}$, thickness $\sim 1 \text{ mm}$) could be consistently loaded with $\sim 1.1 \text{ mg}$ of FLG using the above growth parameters. To induce defects, the FLG coated Ni foams were exposed to varying powers (25 W, 50 W, 75 W, and 100 W) of Ar plasma in a Plasma Etch plasma-cleaning chamber for 60 s at a chamber pressure of $\sim 100 \text{ mTorr}$.

The pristine and plasma etched FLG were coated with a 5 wt% solution of polymethyl methacrylate dissolved in propyl acetate to improve the structural integrity of the foams, and consequently improve the cell performance by creating a hydrophobic layer on the cathode surface [30,31]. The Ni foam which served as the sacrificial substrate was then etched away by submerging the samples in 5 M HCl for $\sim 12 \text{ h}$, after which they were rinsed with a 0.25 M KOH solution to remove the residual HCl. Finally, the samples were rinsed with DI water and dried thoroughly overnight in an oven (120°C) along with the Al foil anodes and glass fiber separators.

The EMI- AlCl_4 ionic liquid electrolyte was prepared by combining AlCl_3 with EMICl in a 1.3:1 M ratio. This ratio has been shown to yield nearly equal amounts of AlCl_4^- and Al_2Cl_7^- anions, which are needed for the initial intercalation into the FLG foam cathode and plating on the Al anode, respectively [20]. Prior to combining the components, EMICl was heated under vacuum at 140°C for at least 24 h to remove any residual moisture. The ionic liquid components were mixed in an Ar filled glove box that contained less than 10 ppm oxygen and water. A schematic for the cell construction is shown in Fig. 1a. All components were assembled into pouch cells using aluminized plastic as the container and Ni tabs (MTI Corp.) as current collectors. Each cell was loaded with $\sim 0.5 \text{ ml}$ of electrolyte prior to sealing.

The DFT calculations were carried out using Quantum ESPRESSO. The approach included the Van der Waals interaction in DFT-D2 under a generalized gradient approximation (GGA) of the exchange correlation functional. The cell size for each graphene layer was chosen to be 4×4 unit cells. The ultrasoft pseudopotential (Rappe Rabe Kaxiras Joannopoulos) was used for all species with GGA. The energy cutoff for the wave function and the charge are 35 Ry and 350 Ry, respectively. The structure containing intercalated AlCl_4^- within two graphene layers was fully relaxed until all force components were smaller than 10^{-3} Ry/Bohr , in order to obtain the exact position and orientation for the molecule. The region between the graphene layers was sliced into 1000 planes parallel to graphene and the charge transfer curve was obtained by computing the charge averaged over each plane.

Electrochemical characterization of the cells was carried out using a Gamry Reference 3000, Keithley 2400 source meter and a Solartron 1470 battery test unit. The Raman spectra were collected using a Renishaw InVia micro-Raman spectrometer (50x objective) with a 532 nm diode laser (Crystalaser). In situ Raman measurements were accomplished by assembling a cell on a glass microscope slide and sealing the edges with epoxy.

3. Results and discussion

Fig. 1a shows a schematic of the cells which were used for all trials. The FLG foam cathodes used in Fig. 1 are either pristine or were exposed to varying intensities of Ar plasma for 60 s as indicated in the figure legend. The plasma treatment serves to induce pores and defects in the surface of the FLG, which could possibly alter the intercalation behavior as reflected by a change in voltage or capacity. Representative CV curves and charge/discharge responses for AIBs with pristine and plasma treated cathodes are displayed in Fig. 1b. Three peaks located at ~ 1.9 , 2.1, and 2.38 V are observed in the CV plots while charging. These voltage values correspond to the onset of the charging plateaus displayed in Fig. 1c and d. The corresponding discharge valleys are located at 2.2 V for the charging peak at 2.38 V while a broad valley appears at 1.9 V encompassing the 1.9 and 2.1 V charging peaks. The dashed lines in the plots serve as a reference points to illustrate that

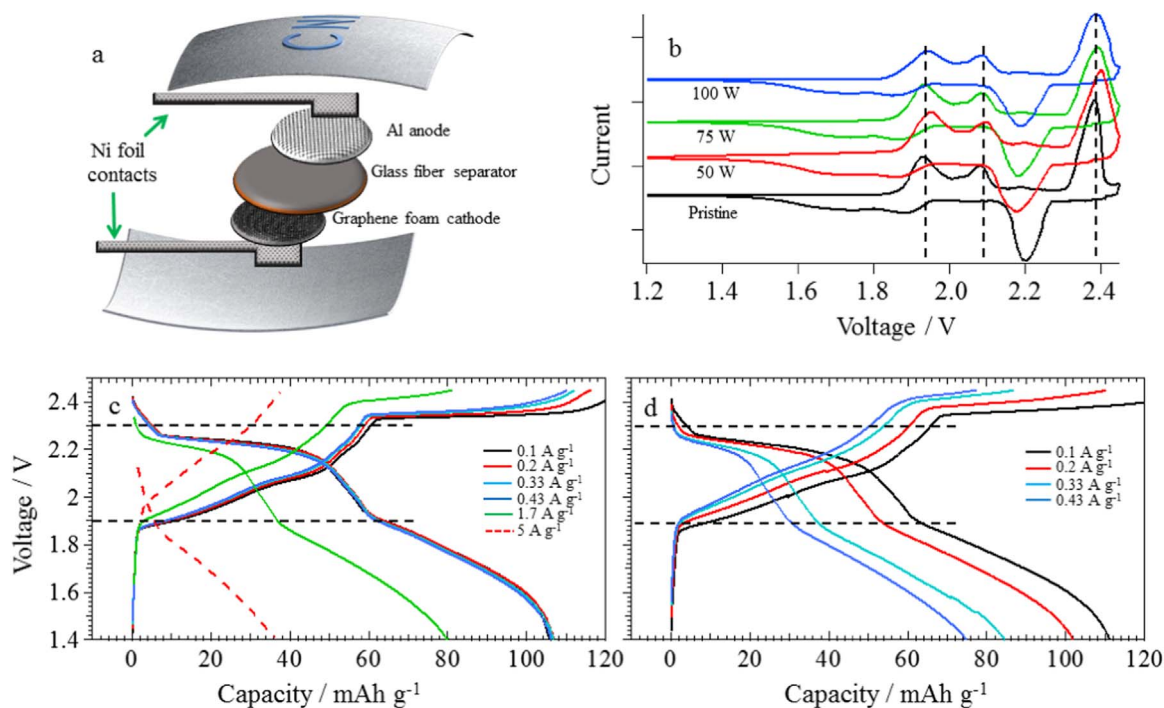


Fig. 1. a) A schematic showing the components of an Al-ion battery (AIB). The upper and lower sheets are aluminized plastic. b) Cyclic voltammograms of AIBs with pristine and plasma treated FLG foam cathodes. The dashed lines correspond to redox processes in the AIB. c) and d) Charge/discharge characteristics for AIBs with a pristine and a 100 W plasma treated cathode, respectively. The dashed lines correspond to the peaks shown in panel b.

there is no significant difference in peak voltage or voltage plateaus between different cathodes. It should be noted that for plasma treated cathodes, the capacity was observed to decrease at a faster rate with increasing discharge current densities than was seen for their pristine counterparts. Previous work done on Li intercalation into graphite showed similar peaks in the CV curves, and it was found through x-ray diffraction (XRD) measurements that they correspond to the onset of staging as the graphite transitions from a high-stage or dilute stage-one GIC to a stage-one GIC [32–34]. As evidenced by the Raman spectra, we deduce that the three redox peaks in the CV for the FLG foam cathode in AIB correspond to staging of the AlCl_4^- anions ultimately leading to a stage-one intercalated FLG.

Raman spectroscopy has been widely used for monitoring charge transfer processes in both donor and acceptor GICs [35–41]. The in-plane vibrations of C atoms with E_{2g2} symmetry in graphite appear as the so-called graphitic or G-band at $\sim 1585 \text{ cm}^{-1}$ in the Raman spectrum. The G-band is highly sensitive to both charge transfer and changes in interlayer interactions during intercalation/de-intercalation. For acceptor GICs, the formation of a dilute stage-one GIC where each layer is sparsely occupied by intercalant is associated with a steady upshift in the G-band frequency from its initial position of $\sim 1585 \text{ cm}^{-1}$. Sudden changes in the graphene layer stacking caused by staging and the associated stresses result in a discrete split of the G-band. The interior unperturbed graphene layers will continue to exhibit a $\sim 1585 \text{ cm}^{-1}$ (E_{2g2i}) mode while the bounding layers adjacent to the intercalant ions display a peak at an upshifted discrete frequency (E_{2g2b}). The degree of the shift is dependent upon the stage of intercalation. A diagram illustrating the graphite interior layers, bounding layers and intercalant staging is shown in Fig. S1.

Fig. 2a and b show the in situ Raman spectra obtained for an FLG foam cathode during a typical charge (a) and discharge (b) cycle. While charging, no shift in the G-band frequency is observed below 1.8 V. A slight upshift is evident as the voltage increases to 1.9 V (corresponding to the first redox peak in Fig. 1b) at which point the G-band splits into two Raman modes for the reasons explained above, the second peak appearing at 1603 cm^{-1} being the E_{2g2b} mode. The upshift in peaks

observed during charging is due to charge extraction from graphene layers in the FLG foam by the intercalated AlCl_4^- ions, indicating an acceptor GIC type behavior [42]. The splitting of the G-band located at $\sim 1585 \text{ cm}^{-1}$ at 1.9 V is due to the onset of ordered staging where intercalate layers influence the frequency of the E_{2g2i} mode, leading to a discrete upshift by 18 cm^{-1} to 1603 cm^{-1} (E_{2g2b} mode). As charging continues past 1.9 V, the GIC transitions to lower stages (i.e., more intercalation leading to more bounding layers) as seen by the diminishing intensity of the E_{2g2i} mode accompanied by a continual upshift in E_{2g2b} mode frequency, which was initially located at $\sim 1603 \text{ cm}^{-1}$. The E_{2g2i} mode disappears as the voltage reaches 2.1 V, which corresponds to the second redox peak observed in Fig. 1b, indicating that interior layers no longer exist and a stage-two GIC is formed [43]. Beyond this point during charging, the voltage rises rapidly, and the E_{2g2b} mode intensity begins to diminish with a concomitant increase in the intensity of a new Raman mode at $\sim 1635 \text{ cm}^{-1}$ (Fig. 2a). The emergence of this new E_{2g2b} mode at $\sim 1635 \text{ cm}^{-1}$ marks a transition from a stage-two to a stage-one GIC, and its corresponding signature is the top most plateau in the charging curve occurring at $\sim 2.3 \text{ V}$ (Fig. 1c) and the largest peak in the CV profile (Fig. 1b).

The total shift of the E_{2g2} mode during charging was found to be $\sim 49 \text{ cm}^{-1}$ for AIBs comprised of pristine FLG foam cathodes with the maximum frequency being 1634 cm^{-1} . This trend in the upshift and splitting of the E_{2g2} mode is in excellent agreement with the trends exhibited by other acceptor GICs (Fig. 2c), which was originally compiled by Dresselhaus and Dresselhaus [44]. The overlaid data in Fig. 2c confirmed that our fully charged FLG foam cathodes were indeed stage-one GICs. Fig. 2d correlates the staging (as determined through Raman spectroscopy) with the CV response for an AIB comprised of pristine FLG foam cathodes. Notably, both Raman and CV data strongly indicate that the charge-discharge processes are highly reversible, and that the EMI- AlCl_4 system is capable of reversible stage-one intercalation with the FLG cathode yielding good cell performance. Similar shifts in the Raman spectra were observed during the discharging process (Fig. 2b). The in situ Raman spectra for an AIB comprised of a 100 W plasma treated FLG foam cathode is shown in

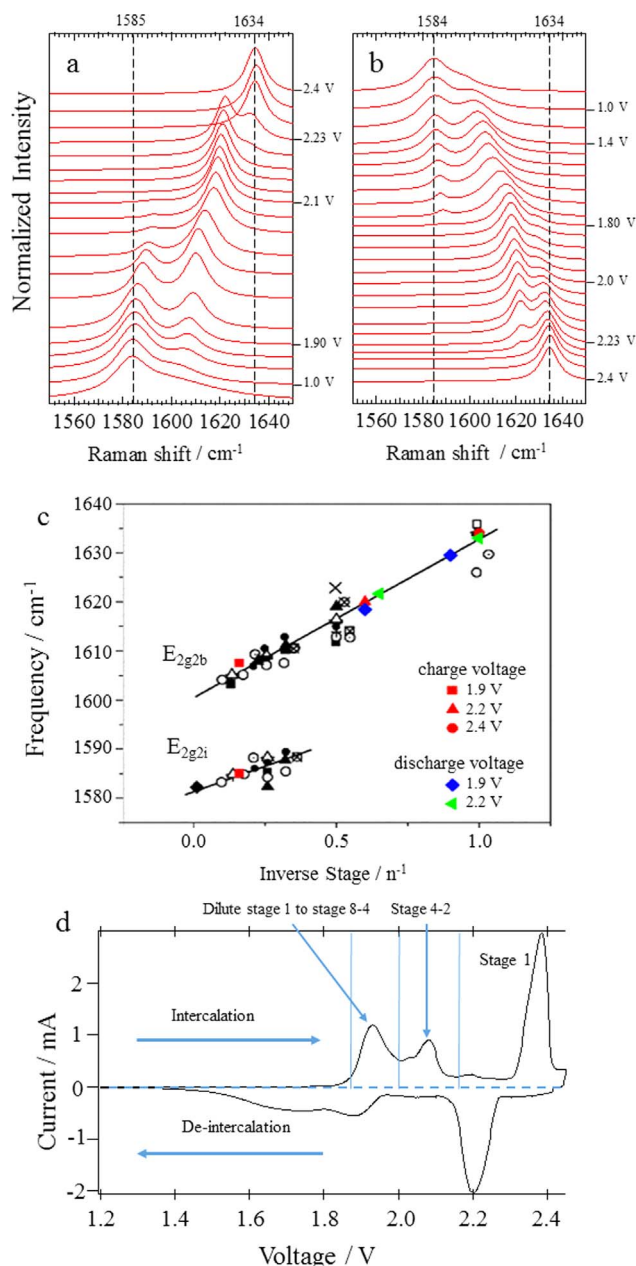


Fig. 2. a) and b) Raman spectra of the FLG cathode during the charge (a) and discharge (b) process. c) A further confirmation of a stage-one GIC is evident when the peak positions (from panels a and b) are overlaid on the universal plot for G-band shifts as a function of reciprocal stage index for acceptor type GICs (taken from Ref. [44]). d) The voltages at which peak current values are obtained track well with the onset of the G-band splitting events, as well as the charge/discharge plateaus shown in Fig. 1.

Fig. S2. The spectra exhibit similar characteristics to those of the pristine examples depicted in Fig. 2a and b, and the Raman shifts also fall on the universal acceptor plot to coincide with a stage-one GIC. No differences in the magnitude of peak shifts are seen between pristine and plasma treated samples indicating that surface defects do not significantly affect the intercalation process. However, as discussed below, the energy and power densities of the 100 W plasma treated FLG cathode is poor compared to the pristine FLG.

The acceptor nature of the AlCl_4^- ion is further demonstrated by our DFT model as shown in Fig. 3. The AlCl_4^- ion is positioned between two layers of Bernal stacked graphene, each containing 32 carbon atoms. Upon relaxation of the system, charge is transferred from the graphene sheets to the chlorine atoms of the AlCl_4^- molecule. As shown in Fig. 3b, we find that the charge is uniformly depleted from carbon atoms

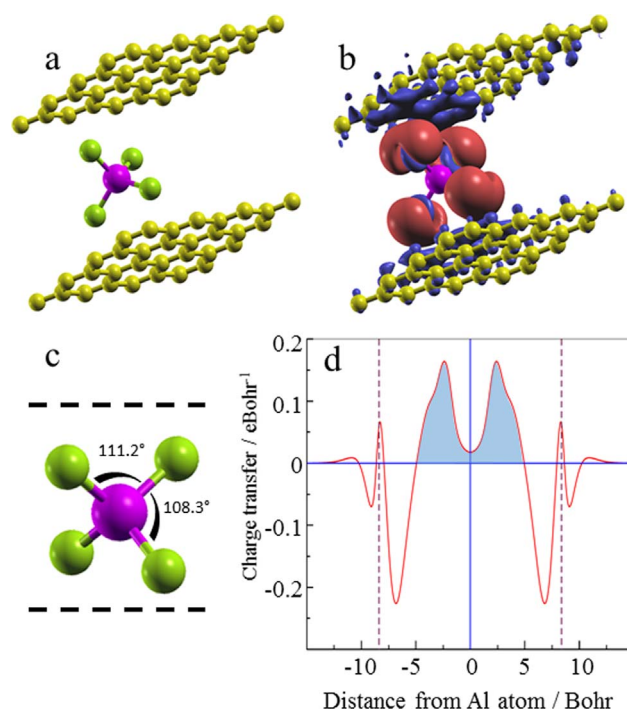


Fig. 3. DFT model of charge transfer between graphene layers and AlCl_4^- intercalant ion. a) and b) show the system before and after relaxation respectively. Negative charge is transferred from the blue regions to the red. c) Bond angles of the distorted AlCl_4^- ion oriented between two graphene planes (dashed lines). The unperturbed bond angles in AlCl_4^- are 109.5°. d) Charge transfer distribution as a function of distance from the central Al atom, the dashed lines marking the position of the graphene planes. The shaded area was integrated to obtain the net charge transfer.

present within the geometrical shadow of AlCl_4^- ion. We also observe that the tetrahedral structure of AlCl_4^- is slightly deformed upon intercalation (Fig. 3c). The amount of transferred negative charge is determined by integrating the area between the zero-energy intercept points of the charge transfer curve (~ -5 to 5 Bohr) indicated by the shaded area in Fig. 3d, yielding 0.8 e per intercalant ion.

Fig. 4a is a Ragone plot which summarizes the performance of AIBs with FLG cathodes. The specific energy values for the AIBs were determined by integrating the areas under the plateaus shown in the voltage vs. capacity plots in Fig. 1c and d, and the specific power was calculated by dividing the specific energy with the discharge time. Fig. 4a also displays the performance of AIBs demonstrated by other researchers in the recent literature [11,25]. The power and energy densities of their AIBs were determined by integrating the capacity curves provided in their data. We find that our AIBs with pristine FLG show a marked increase in power and energy density over those previously published.

We attribute this increased performance to the robustness of our FLG cathodes, which allow intercalation to a fully stage-one GIC unlike other studies. For example, in the study by Yu et al., their CV data did not display the three distinct redox peaks during charging (cf. Fig. 1b), and their galvanostatic discharge plots only showed a very weak plateau at ~ 2.1 V, indicating that a stage-one GIC was not achievable under their experimental conditions, which adversely affected the cell performance. In the work by Lin et al., they used XRD measurements of a charged cathode and determined it to be a stage-four GIC when charged. This was corroborated by their in situ Raman data taken while the cell was charged to 2.42 V. The G-band of their cathode was located at ~ 1625 cm⁻¹ while charged, indicating that a stage-one GIC was not realized under their experimental conditions either.

We also evaluated the stability of a pristine AIB, wherein the cathode reaches full stage-one intercalation, by using galvanostatic cycling at 3 A g^{-1} and a peak voltage of 2.4 V. As shown in Fig. 4b, our

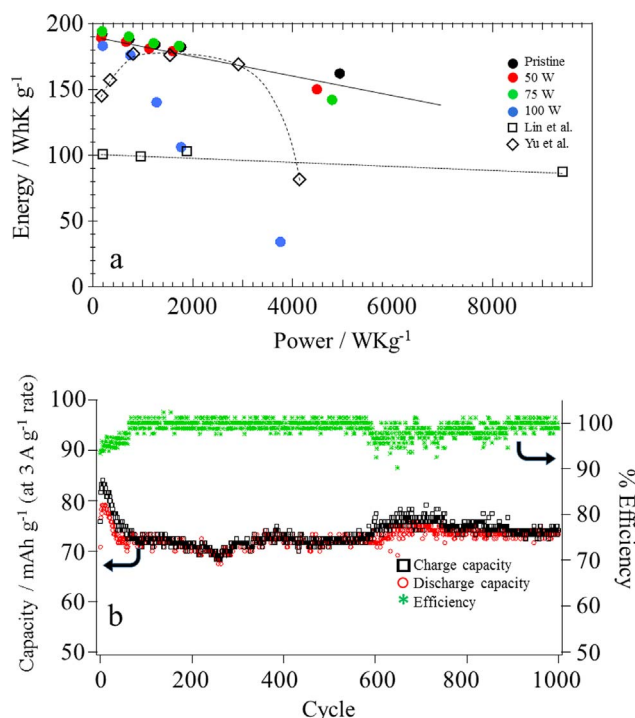


Fig. 4. a) Ragone plot for AIBs made using pristine and plasma treated FLG foam cathodes. The legend shows the power of the plasma to which the FLG was exposed. The poor performance for the cell which uses the 100 W cathode is due to structural damage caused by the high plasma power. Data for AIBs reported by Lin et al. (Ref. [7]), and Yu et al. (Ref. [27]) are also included in the Ragone plot for comparison. b) Charge/discharge cycling of a pristine AIB subjected to 1000 cycles at a rate of 3 A g^{-1} with a potential limit of 2.4 V.

AIBs yielded a coulombic efficiency near 100% up to 1000 cycles with minimal loss of capacity. The initial increase in capacity has yet to be investigated but could be related to chemistry at the surface of the Al anode. The AIBs require no conditioning since no surface-electrolyte interface layer is formed using this ionic liquid electrolyte.

Though the spectroelectrochemical signature of the FLG foam cathode exposed to 100 W plasma is identical to the pristine cathode, its energy and power densities deteriorate rapidly. We attribute this deteriorated performance to the poor connectivity of graphene grains due to damage induced by plasma treatment. It is well known that defects in the graphene lattice increase sheet resistivity [45–48], and the same can be inferred from Fig. S3 which displays Nyquist plots at several voltages for pristine FLG and FLG treated with 100 W plasma. The semicircles of the plasma treated FLG are larger than those exhibited by the pristine FLG, indicating greater charge-transfer resistance in the former. Furthermore, the semicircles also change as the voltage is increased for the plasma treated FLG, with the clear formation of a second semicircle at higher frequencies for higher voltage values, a trend that was absent for pristine FLG. Indeed, we found that treating the cathodes at the maximum power of 100 W for longer periods of time resulted in the ablation of all carbon from the Ni foam substrate, prompting a further study to investigate the structure of the FLG foam when exposed to plasma. FLG grown on Ni foil was used in this experiment because the smooth foil surface allows much easier observation of the FLG before and after plasma treatment. In Fig. 5, the top image shows FLG grown on Ni foil while the bottom image is the same FLG following 30 s exposure to 100 W Ar plasma. The brighter areas of the substrate correspond to exposed Ni while the darker areas are FLG, demonstrating the ablation of carbon material when the FLG is exposed to the high power plasma. Their corresponding Raman spectra are shown to the right where the so-called disorder or *D*-band ($\sim 1350 \text{ cm}^{-1}$) is very prominent for the plasma treated sample. The *G'*-band located at 2700 cm^{-1} indicates the presence of

multiple layers, concurring with our atomic force microscopy (Fig. S4), which shows the FLG to be $\sim 5 \text{ nm}$ thick. The ablation of FLG due to excessive plasma treatment, as shown in Fig. 5, would deteriorate structural integrity and electrical connectivity within the FLG foam cathode, ultimately resulting in a loss of capacity. Raman spectra were also obtained for other plasma intensities and can be found in Fig. S5 where it is seen that the *D*-band grows progressively larger with increasing plasma intensity.

In addition to the structural defects, we find that chemical defects such as N-dopants impede intercalation and are thus detrimental to the cell performance. Nitrogen dopants in graphene are known to support three main configurations. In the graphitic configuration, carbon atoms are substituted with nitrogen without disrupting the lattice, while for the pyridinic and pyrrolic configurations, vacancies in the lattice are necessary. Based on our previous studies in N-doped graphene, and the synthesis conditions used in this study, we infer that the N-dopants are primarily in the graphitic doping configuration [24,49,50]. Fig. 6a shows the charge/discharge curves for N-doped FLG cathodes which are seen to lack the double plateaus of their un-doped counterparts (cf. Fig. 1c and d). Appreciable intercalation could only be achieved at the lower charge rates of 0.1 and 0.3 A g^{-1} . The single plateau begins only once the voltage has reached $\sim 2.1 \text{ V}$ and then slowly increases, while the discharge is very quick and delivers poor capacity. This intercalation showed a very flat plateau and was accompanied by gas evolution, both of which indicate breakdown of the intercalated ions. The reaction of the ionic liquid that occurs once intercalation begins at $\sim 2.2 \text{ V}$ could be due to catalytic activity of the nitrogen dopant sites within the graphene layers. The catalytic properties of N-doped graphene for oxidation and reduction have been well documented and could lead to the production of chlorine gas once intercalation of the AlCl_4^- anions begins, which would hamper the intercalation process [51–56]. As the reactivity of nitrogen defects is known to vary depending on the configuration, it is expected that different configurations would lead to varying degrees of catalytic activity during intercalation. However, such an investigation is beyond the scope of the current work. Incomplete intercalation is indicated by the cyclic voltammogram and in situ Raman spectra in Fig. 6b and c respectively. Cyclic voltammetry was carried out at 3 mV s^{-1} and shows only broad peaks, lacking the sharp peak of a stage-one transition as observed for pristine FLG in Fig. 2d. Likewise, the Raman spectra only show a single split of the *G*-band while charging. The split occurs at $\sim 2.1 \text{ V}$, significantly higher compared to that of un-doped FLG (cf. Fig. 2a). The $\text{E}_{2\text{g}2\text{i}}$ mode originating at 1584 cm^{-1} is seen to remain throughout the charging process, showing the N-doped FLG cathode is only in a mixed phase of staging and fails to achieve even stage-two intercalation. Based on our DFT calculations in Fig. 3, we tentatively attribute the poor intercalation to greater repulsion between electron rich N-dopant sites and highly electronegative Cl ions in AlCl_4^- intercalant. A detailed DFT and Raman analysis of N-doped FLG cathodes will be published elsewhere.

4. Conclusions

To conclude, we demonstrated AIBs comprised of FLG foam cathodes whose cell performance exceeded similar systems reported in the literature by achieving stage-one intercalation within the nominal voltage window, thereby fully utilizing the gallery space between graphene layers. Specifically, the excellent correlation observed between our CV plots and in situ Raman spectroscopy during charge/discharge cycles strongly implies that the superior cell performance demonstrated in this study stems from the reversible intercalation/de-intercalation processes supported by the FLG foam cathodes. Notably, we demonstrated AIBs with high energy and power densities ($\sim 200 \text{ Wh kg}^{-1}$ at 200 W kg^{-1} and $\sim 160 \text{ Wh kg}^{-1}$ at 5000 W kg^{-1}) that exhibit a slow decrease in energy at higher power densities. From the CV plots in Fig. 1b, it is seen that the peak current potentials do not deviate significantly between cells comprised of pristine or plasma

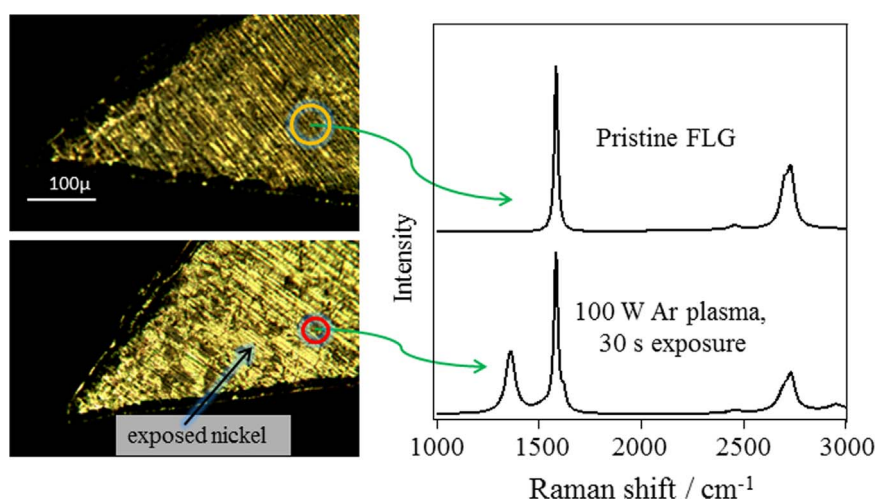


Fig. 5. The top optical microscope image shows FLG on Ni foil next to its associated Raman spectrum. Notice that the Ni foil appears dark and the Raman *D*-band is absent signifying the high quality of the FLG. The bottom optical image shows the same area after being exposed to 100 W Ar plasma for 30 s revealing the relatively brighter surface of the Ni foil.

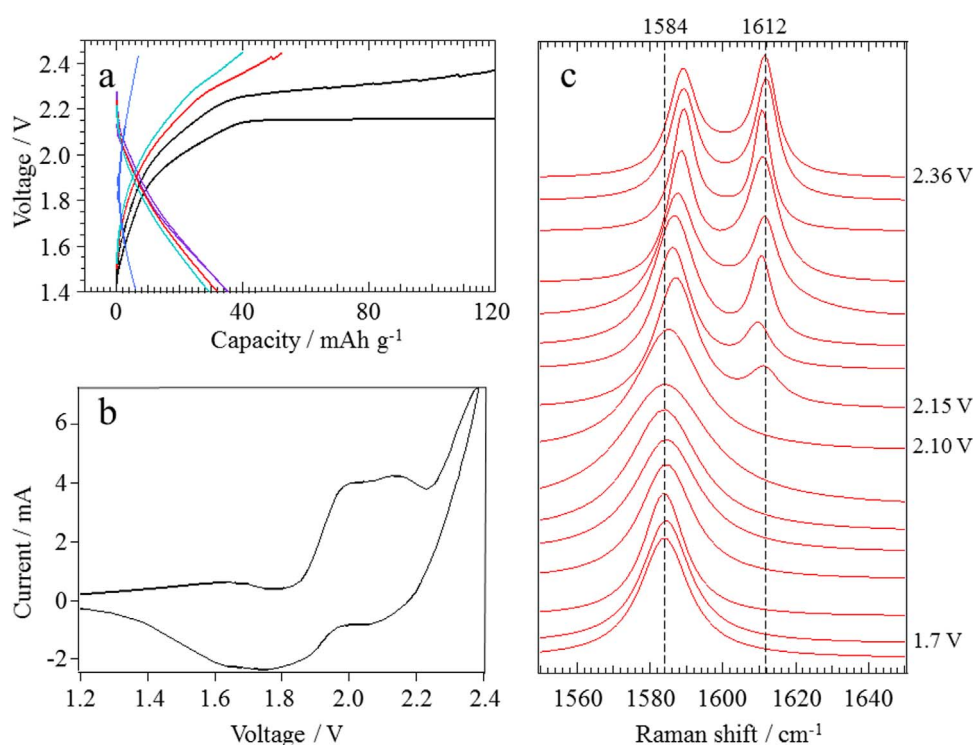


Fig. 6. Cell performance when using an N-doped FLG cathode. a) charge/discharge curves at various current densities. Current densities increase from right to left as 0.1, 0.3, 0.6, 1, and 1.5 A g⁻¹. b) the cyclic voltammogram shows broad peaks and does not display the third sharp peak (~ 2.38 V) corresponding to stage-one transition in pristine cathodes (see Fig. 2d). c) In situ Raman spectra obtained during charging show only one *E*_{2g2b} peak and the *E*_{2g2i} peak does not vanish before the cutoff voltage is reached, showing a fully stage-two or stage-one intercalation could not be reached.

treated FLG foams at different plasma powers, confirming that the presence of in-plane surface defects in FLG cathodes does not alter the staging processes. Likewise, in terms of energy and power densities (Fig. 4), the FLG foams treated at 50 and 75 W exhibited similar performances as the pristine FLG foam, while FLG foams treated at 100 W showed a comparatively poor performance. Three key insights into AIB batteries have been provided: i) it is necessary to reach stage-

one FLG to achieve high energy and power density, which was confirmed using CV curves, DFT calculations, and Raman spectroscopy, ii) the AIB performance and the ion intercalation are insensitive to in-plane surface defects as long as the structural integrity and electrical connectivity of the FLG cathode are retained, and iii) chemical defects such as N-dopants preclude stage-one intercalation and lead to poor performance.

Acknowledgements

We would like to acknowledge the Scalable Nanomanufacturing award #CMMI-1246800 for funding, and Longyu Hu for graciously acquiring the AFM images. R.P. and A. M. R. are thankful to the Watt Family Innovation Center, Clemson University and Haworth, Inc. for their support.

Appendix A. Supplementary material

Supplementary data associated with this article can be found in the online version at <http://dx.doi.org/10.1016/j.nanoen.2017.06.038>.

References

- [1] M.Z. Jacobson, M.A. Delucchi, *Energy Policy* 39 (2011) 1154–1169.
- [2] M. Fleischer, *Circ. Geol. Surv.* 285 (1953) 1–6.
- [3] N. Jayaprakash, S.K. Das, L.A. Archer, *Chem. Commun.* 47 (2011) 12610–12612.
- [4] J.V. Rani, V. Kanakiah, T. Dadmal, M.S. Rao, S. Bhavanarushi, *J. Electrochem. Soc.* 160 (2013) A1781–A1784.
- [5] H. Sun, W. Wang, Z. Yu, Y. Yuan, S. Wang, S. Jiao, *Chem. Commun.* 51 (2015) 11892–11895.
- [6] P.R. Gifford, J.B. Palmisano, *J. Electrochem. Soc.* 135 (1988) 650–654.
- [7] M. Chiku, H. Takeda, S. Matsumura, E. Higuchi, H. Inoue, *ACS Appl. Mater. Interfaces* 7 (2015) 24385–24389.
- [8] H. Wang, Y. Bai, S. Chen, X. Luo, C. Wu, F. Wu, J. Lu, K. Amine, *ACS Appl. Mater. Interfaces* 7 (2015) 80–84.
- [9] J. Hu, J. Ma, L. Wang, H. Huang, L. Ma, *Powder Technol.* 254 (2014) 556–562.
- [10] W. Wang, B. Jiang, W. Xiong, H. Sun, Z. Lin, L. Hu, J. Tu, J. Hou, H. Zhu, S. Jiao, *Sci. Rep.* 3 (2013) 2093–2104.
- [11] M.C. Lin, M. Gong, B.G. Lu, Y.P. Wu, D.Y. Wang, M.Y. Guan, M. Angell, C.X. Chen, J. Yang, B.J. Hwang, H.J. Dai, *Nature* 520 (2015) 325.
- [12] R. Raccichini, A. Varzi, S. Passerini, B. Scrosati, *Nat. Mater.* 14 (2014) 271–279.
- [13] F. Bonaccorso, L. Colombo, G. Yu, M. Stoller, V. Tozzini, A.C. Ferrari, R.S. Ruoff, V. Pellegrini, *Science* 347 (80) (2015).
- [14] C. Hu, L. Song, Z. Zhang, N. Chen, Z. Feng, L. Qu, *Energy Environ. Sci.* 8 (2015) 31–54.
- [15] W. Lv, Z. Li, Y. Deng, Q.-H. Yang, F. Kang, *Energy Storage Mater.* 2 (2016) 107–138.
- [16] J.S. Wilkes, J.A. Levinsky, R.A. Wilson, C.L. Hussey, *Inorg. Chem.* 21 (1982) 1263–1264.
- [17] A.A. Fannin, L.A. King, J.A. Levinsky, J.S. Wilkes, *J. Phys. Chem.* 88 (1984) 2609–2614.
- [18] J.J. Auborn, Y.L. Barberio, *J. Electrochem. Soc.* 132 (1985) 598–601.
- [19] P.K. Lai, M. Skyllas-Kazacos, *J. Electroanal. Chem.* 248 (1988) 431–440.
- [20] H.A. Oye, M. Jagtoyen, T. Oksefjell, J.S. Wilkes, *Mater. Sci. Forum* 73–75 (1991) 183–190.
- [21] T. Jiang, M.J.C. Brym, G. Dube, A. Lasia, G.M. Brisard, *Surf. Coat. Technol.* 201 (2006) 1–9.
- [22] S.C. Jung, Y.J. Kang, D.J. Yoo, J.W. Choi, Y.K. Han, *J. Phys. Chem. C* 120 (2016) 13384–13389.
- [23] M.S. Wu, B. Xu, L.Q. Chen, C.Y. Ouyang, *Electrochim. Acta* 195 (2016) 158–165.
- [24] J. Zhu, A.S. Childress, M. Karakaya, S. Dandeliya, A. Srivastava, Y. Lin, A.M. Rao, R. Podila, *Adv. Mater.* 28 (2016) 7185–7192.
- [25] X. Yu, B. Wang, D. Gong, Z. Xu, B. Lu, *Adv. Mater.* 29 (2016) 1604118.
- [26] L. Zhang, L. Chen, H. Luo, X. Zhou, Z. Liu, *Adv. Energy Mater.* (2017) 1700034.
- [27] K. Share, A.P. Cohn, R. Carter, B. Rogers, C.L. Pint, *ACS Nano* 10 (2016) 9738–9744.
- [28] H. Wang, C. Zhang, Z. Liu, L. Wang, P. Han, H. Xu, K. Zhang, S. Dong, J. Yao, G. Cui, A.K. Geim, M. Rühle, D.L. Carroll, *J. Mater. Chem.* 21 (2011) 5430.
- [29] Z.-S. Wu, W. Ren, L. Xu, F. Li, H.-M. Cheng, *ACS Nano* 5 (2011) 5463–5471.
- [30] Z. Chen, W. Ren, L. Gao, B. Liu, S. Pei, H.-M. Cheng, *Nat. Mater.* 10 (2011) 424–428.
- [31] R. Santhanam, M. Noel, *J. Power Sources* 63 (1996) 1–6.
- [32] M.D. Levi, D. Aurbach, *J. Electroanal. Chem.* 421 (1997) 79–88.
- [33] M.D. Levi, E.A. Levi, D. Aurbach, *J. Electroanal. Chem.* 421 (1997) 89–97.
- [34] M. Noel, V. Suryanarayanan, *J. Power Sources* 111 (2002) 193–209.
- [35] J. Song, D. Chung, P. Ekiund, M. Dresselhaus, *Solid State Commun.* 20 (1976) 1111–1115.
- [36] S.A. Solin, *Mater. Sci. Eng.* 31 (1977) 153–156.
- [37] R.J. Nemanich, S.A. Solin, D. Guerard, *Phys. Rev. B* 16 (1977) 2965–2972.
- [38] J.C. Chacón-Torres, L. Wirtz, T. Pichler, *ACS Nano* 7 (2013) 9249–9259.
- [39] J.C. Chacón-Torres, L. Wirtz, T. Pichler, *Phys. Status Solidi* 251 (2014) 2337–2355.
- [40] N. Jung, N. Kim, S. Jockusch, N.J. Turro, P. Kim, L. Brus, *Nano Lett.* 9 (2009) 4133–4137.
- [41] K. Share, A.P. Cohn, R.E. Carter, C.L. Pint, *Nanoscale* 8 (2016) 16435–16439.
- [42] P.C. Eklund, E.T. Arakawa, J.L. Zarestky, W.A. Kamitakahara, G.D. Mahan, *Synth. Met.* 12 (1985) 97–102.
- [43] M. Inaba, H. Yoshida, Z. Ogumi, T. Abe, Y. Mizutani, M. Asano, *J. Electrochem. Soc.* 142 (1995) 20.
- [44] M.S. Dresselhaus, G. Dresselhaus, *Adv. Phys.* 51 (2002) 1–186.
- [45] C. Gómez-Navarro, R.T. Weitz, A.M. Bittner, M. Scolari, A. Mews, M. Burghard, K. Kern, *Nano Lett.* 7 (2007) 3499–3503.
- [46] W. Tian, W. Li, W. Yu, X. Liu, *Micromachines* 8 (2017) 163.
- [47] N. Gorjizadeh, A.A. Farajian, Y. Kawazoe, *Nanotechnology* 20 (2009) 15201.
- [48] L. Vicarelli, S.J. Heerema, C. Dekker, H.W. Zandbergen, *ACS Nano* 9 (2015) 3428–3435.
- [49] R. Podila, J. Chacón-Torres, J.T. Spear, T. Pichler, P. Ayala, A.M. Rao, *Appl. Phys. Lett.* 101 (2012).
- [50] B. Anand, M. Karakaya, G. Prakash, S.S.S. Sai, R. Philip, P. Ayala, A. Srivastava, A.K. Sood, A.M. Rao, R. Podila, *RSC Adv.* 5 (2015) 59556–59563.
- [51] J. Wu, L. Ma, R.M. Yadav, Y. Yang, X. Zhang, R. Vajtai, J. Lou, P.M. Ajayan, *ACS Appl. Mater. Interfaces* 7 (2015) 14763–14769.
- [52] D.-P. Kim, C.L. Lin, T. Mihalisin, P. Heiney, M.M. Labes, *Chem. Mater.* 3 (1991) 686–692.
- [53] R.A. Sidik, A.B. Anderson, N.P. Subramanian, S.P. Kumaraguru, B.N. Popov, *J. Phys. Chem. B* 110 (2006) 1787–1793.
- [54] J. Liu, D. Takeshi, D. Orejon, K. Sasaki, S.M. Lyth, *J. Electrochem. Soc.* 161 (2014) 544–550.
- [55] S. Li, W. Wang, X. Liu, X. Zeng, W. Li, N. Tsubaki, S. Yu, *RSC Adv.* 6 (2016) 13450–13455.
- [56] Y. Shao, S. Zhang, M.H. Engelhard, G. Li, G. Shao, Y. Wang, J. Liu, I.A. Aksay, Y. Lin, *J. Mater. Chem.* 20 (2010) 7491.



Anthony S. Childress received his B.S. degree in Chemistry from Old Dominion University in the USA. He is currently pursuing a Ph.D. in physics under the supervision of Prof. Rao at Clemson University. His dissertation is focused on the role of defects in energy-related nanomaterials.



Prakash Parajuli received his B.S. and M.S. degrees in physics from Tribhuvan University in Nepal. He is currently pursuing a Ph.D. in physics under the supervision of Prof. Rao at Clemson University. His dissertation is focused on modeling and synthesis of nanomaterials.



Dr. Jingyi Zhu received her B.S. and M.S. degrees in physics from Lanzhou University in China. She earned her Ph.D. in condensed matter physics under the supervision of Prof. Rao at Clemson University. Her dissertation focused on the electrochemical properties of carbon nanomaterials.



Dr. Ramakrishna Podila is an Assistant Professor in physics at Clemson University. He received his M.S. degree in physics from the Indian Institute of Technology in 2007 and a Ph.D. in physics from Clemson in 2011. He worked at the Brody school of medicine, Greenville, NC until 2013, following which he returned to Clemson. His current research is centered on elucidating fundamental optical, electronic, and magnetic properties of nanomaterials, and using them for nanomedicine and energy applications.



Prof. Apparao M. Rao received his Ph.D. in experimental condensed matter physics from the University of Kentucky in 1989 under the tutelage of Prof. P. C. Eklund. He then joined Prof. M. S. Dresselhaus' group at MIT as a postdoctoral associate until 1991. He is currently the R. A. Bowen Professor of Physics, and the Director of Clemson Nanomaterials Institute at Clemson University. He is a Fellow of the American Association for Advancement of Science, and the American Physical Society.